This article has been accepted for publication in IEEE Open Journal of Antennas and Propagation. This is the author's version which has not been fully edited and content may change prior to final publication. Citation information: DOI 10.1109/OJAP.2024.3477318

IEEE Open Journal of Antennas and Propagation

Received XX Month XXXX; revised X Month XXXX; accepted XX Month XXXX. Date of publication XX Month XXXX; date of current version XX Month XXXX.

Digital Object Identifier 10.1109/OAJPE.2020.2976889

Beam Shaping of a Dual-reflector Antenna Using a Reflectarray as Subreflector and Embedded Unit Cell Patterns

MARZIEH MEHRI DEHNAVI[1], AND
JEAN-JACQUES LAURIN[1], SENIOR MEMBER, IEEE

[1]Department of Electrical Engineering, Polytechnique Montréal, Montréal, QC H3T 1J4, Canada

CORRESPONDING AUTHOR: Jean-Jacques Laurin (e-mail: jean.jacques.laurin@polymtl.ca).

This work was supported by the Natural Sciences and Engineering Research Council (NSERC) of Canada.

ABSTRACT This work proposes a phase-only synthesis technique for shaping the beam of a circularly polarized dual-reflector antenna with a subreflector consisting of a reflectarray and a main parabolic reflector. The proposed technique exploits the element patterns of each reflectarray unit cell embedded in the whole system, including a feed horn, a reflectarray, and a main reflector. By using a penalty function that forces only the fitting of the desired and obtained patterns, the algorithm leads to a quasi-random phase distribution on the reflectarray and a poor radiation pattern. A term for minimizing the Laplacian of the phase distribution is added to the penalty function to force a smoothly varying phase distribution on the reflectarray. This modification provides more stable results and yields patterns with desired shapes and regular contours. The beam shaping capability of the algorithm is demonstrated with simulations of a 100-element reconfigurable circularly polarized reflectarray, by controlling independently the 10 dB beamwidth of the antenna in two orthogonal planes The algorithm is also validated experimentally. Beamwidth accuracies vary from 0 to 2.15 degrees.

INDEX TERMS Dual-reflector antenna, reconfigurable sub-reflectarray, beam shaping, beam synthesis, particle swarm optimization, circular polarization

I. INTRODUCTION

High-gain antennas that rely on parabolic reflectors are widely used in long-distance communications [1, 2]. For example, dual-reflector antennas with a main parabolic reflector and reconfigurable subreflector can be used in direct broadcast satellite (DBS) missions with contoured beam requirements while maintaining the high gain and wideband properties of the parabolic dish [3]. In a dual-reflector system, implementing reconfigurability at the subreflector level, for instance by controlling the phase shifts of reflectarray elements, is advantageous from a manufacturing perspective due to the smaller sub-reflectarray size [3]. In addition, it is possible to control the beamwidth, sidelobe level, and null positions adapted to the desired coverage by applying phase-only synthesis [3]. Some efforts have been made to synthesize the beam of linearly polarized dual-reflector antennas with a reconfigurable subreflector by synthesizing the required phase on the sub-reflectarray. In [2], beam scanning was realized by implementing a progressive phase shift (PPS) on the sub-reflectarray, whereas in [4] shaped beams were synthesized by applying phase delays caused by an equivalent ellipsoidal subreflector in a Gregorian system. In [5], scan angles of up to ±6 degrees were achieved. Rather than applying PPS, the phases on the sub-reflectarray are derived from the field reflected by the main reflector (using physical optics) exposed to an incident plane wave originating from the desired scanning direction. Hu *et al.* [6] also applied PPS on a sub-reflectarray to demonstrate beam steering in a system operating in the W band in which no reconfigurability is implemented. This work differs from the state-of-the-art methods in three main aspects. First, it is the only work that includes an experimental demonstration of reconfigurability at the sub-reflectarray level. Second, this is the only case in which circular polarization is used. Third, and more importantly, owing to experimental and fabrication constraints, the size of the reflectarray is much smaller, both in terms of wavelength and number of elements, than the sub-reflectarrays considered in [2-6]. Therefore, local periodicity cannot be assumed to analyze the reflectarray, which makes the phase synthesis techniques used in [4, 5] unusable. In Section IIB and IIC of this paper, we propose a novel approach for calculating and synthesizing the far-field pattern of a dual-reflector system using such a small sub-reflectarray. In this approach, the entire reflectarray is simulated using the method of moments to build an element-

This work is licensed under a Creative Commons Attribution-NonCommercial-NoDerivatives 4.0 License. For more information, see https://creativecommons.org/licenses/by-nc-nd/4

This article has been accepted for publication in IEEE Open Journal of Antennas and Propagation. This is the author's version which has not been fully edited and content may change prior to final publication. Citation information: DOI 10.1109/OJAP.2024.3477318

by-element system response that considers the array edge effects, structural scattering and possible specular reflection. Several beam synthesis algorithms based on phase-only techniques have been reported in literature. These include the projection matrix algorithm (PMA), intersection approach (IA), iterative sampling method, genetic algorithm (GA), and particle swarm optimization algorithm (PSO) [7-12].

IA is one of the most efficient methods for phase-only synthesis of reflectarrays in terms of memory usage, speed, and convergence [8]. Moreover, this method has been used for large reflectarrays [13, 15]. However, it suffers from the local minimum problem.

Unlike the traditional optimization methods, such as the least-square approach for pattern synthesis, GA and PSO algorithms allow the specification of multiple design goals, such as sidelobe level, beamwidth, and null control [10, 14]. PSO has a less complex implementation and requires less computing time than GA while simultaneously running global and local searches [10, 11].

Following the work presented in [15], this study aims to experimentally demonstrate the reconfigurable beam shaping capability of a system that includes a main parabolic reflector and a flat reconfigurable subreflector. As described in [16], mechanically rotated circularly polarized (CP) unit cells were used. However, instead of covering the main reflector, the cells only covered the subreflector, which significantly reduced their number. A new beam synthesis approach based on the superposition of patterns associated with each individual cell of the sub-reflectarray, after reflection from the parabolic dish, is proposed. This approach is easy to implement in a system with a small reconfigurable sub-reflectarray. A PSO-based phase-only synthesis algorithm [17] is used to realize the desired beams. The proposed technique can shape and steer the main beam of an antenna. However, for brevity, this study addresses only beam shaping. Section II introduces a modified penalty function used in the PSO algorithm for beam synthesis of the proposed dual-reflector system. The performance of the algorithm is explored in Section III by synthesizing shaped beams, and the proposed approach is validated experimentally in Section IV.

II. BEAM SYNTHESIS BASED ON SUB-REFLECTARRAY ELEMENT PATTERNS

A. DUAL-REFLECTOR ANTENNA STRUCTURE

The structure of the antenna used to illustrate the proposed synthesis method is shown in Fig. 1. The antenna includes a horn, a reconfigurable sub-reflectarray (RSR) for which the phases must be optimized, and a solid parabolic dish. The dimensions of the horn and subreflector were selected to comply with the limitations of the fabrication and test equipment available for experimental validation.

Many techniques to realize reconfigurable reflectarrays or intelligent surfaces have been studied. Recent works, such as [18, 19] use 1-bit PIN diode based unit cells, varactor diodes as in [20], or tunable liquid crystals [21].

For reflectarrays used as a subreflector, a recent paper by Kulkarni *et al.* [22] present a Cassegrain antenna in which

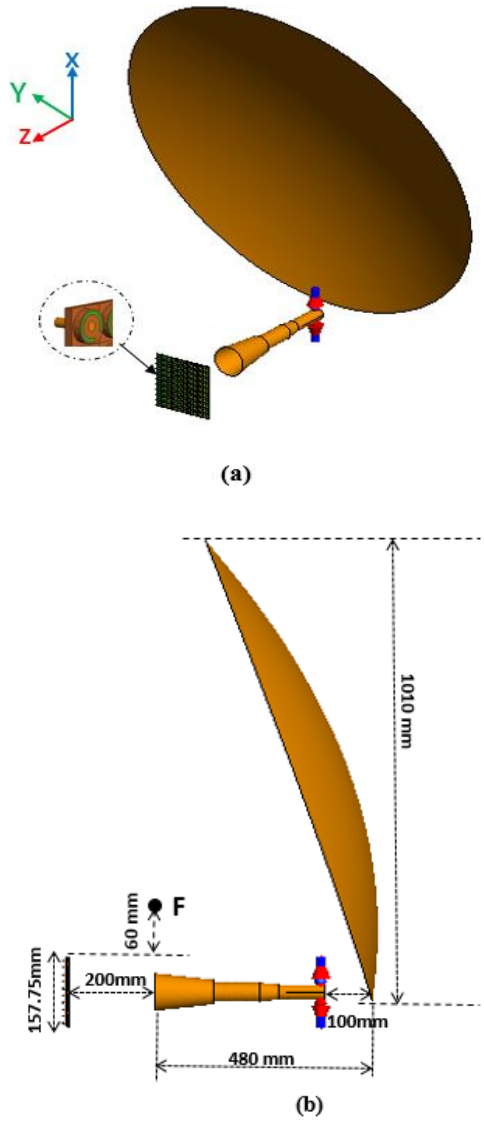

FIGURE 1. (a) Dual-reflector antenna including a horn, a sub-reflectarray, and a solid parabolic dish. The unit cell in the dotted circle shows the front view of the reflectarray element. (b) Side view of (a) with dimensions.

the hyperboloidal subreflector is replaced with a metasurface. No beam shaping is applied, and the unit cell is narrow-band. In order to address the needs of satellite communications, reconfigurable elements with circular polarization, low loss, large bandwidth and high power handling are needed. For this reason, we have chosen for this work to use the mechanically-reconfigurable unit cells described here. The size of the RSR is $3.67\lambda \times 3.67\lambda$ (λ=42.8 mm at the design frequency of 7 GHz) with 10×10 elements with a periodicity of 15.75 mm (0.365 λ) in a square lattice. The RSR unit cell introduced in [23] is illustrated in Fig. 2, and Table 1 lists the relevant dimensions. Each element consists of a small disk-shaped printed circuit implementing the Pancharatnam-Berry phase: mechanical rotation by an angle of ψ about the local direction normal to the RSR causes a variation of 2ψ in the phase of the signal

This work is licensed under a Creative Commons Attribution-NonCommercial-NoDerivatives 4.0 License. For more information, see https://creativecommons.org/licenses/by-nc-nd/4

This article has been accepted for publication in IEEE Open Journal of Antennas and Propagation. This is the author's version which has not been fully edited and content may change prior to final publication. Citation information: DOI 10.1109/OJAP.2024.3477318

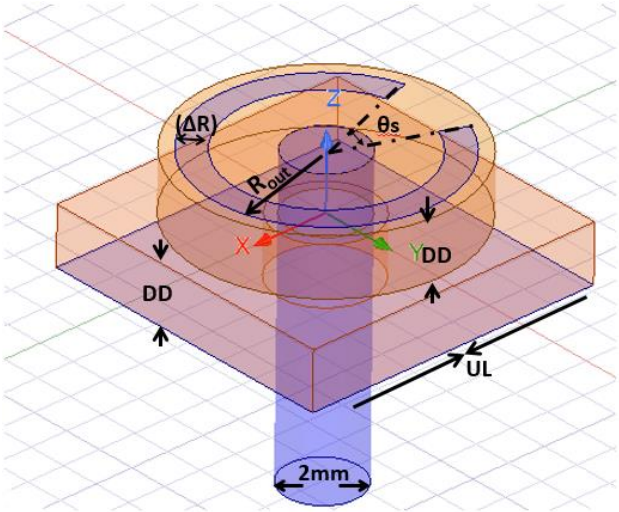

FIGURE 2. Unit cell structure (in the figure, the element rotation angle is $\psi = 0$)

reflected by the corresponding RSR cell, without changing the sense of CP rotation.

A board driving 100 low-cost servo motors (SER0039 from DFRobot) with 1-degree resolution on ψ was designed. Control is realized with an Atmega328P microcontroller, using external current drivers (PCA9685 from Adafruit). Each motor is attached to the 2-mm shaft of the unit cell visible in Fig. 2, in order to rotate the top disk.

Fig. 3a shows the amplitude of the reflected wave under normal incidence illumination for different rotation angles covering the 360-degree range. These simulation results were obtained using Ansys-HFSS. The co-polarized curves show the reflection coefficient Γ_{RR}, corresponding to the level of reflected right-hand polarization for an incident right-handed polarized signal. The cross-polarized curves show Γ_{LR}, which corresponds to the level of reflected left-hand polarization for an incident right-handed polarized signal.

TABLE 1. Unit cell structure parameters

Parameter	Value
Dielectric-Thickness (Duroid 6002) (DD)	3.048 mm
Θs (Gap)	40 degrees
Line Width (ΔR)	1.4 mm
R_{out}	6.3 mm
Unit Cell Size (UL)	15.75 mm
Dielectric-Cylinder Radius (CR)	7 mm

As shown in Fig. 3a, Γ_{LR} is 20 dB or more below Γ_{RR} over a frequency range of 5.9 to 7.3 GHz (21%). Fig. 3b shows the phase of Γ_{RR} as a function of the element rotation angle for three frequency points: 6.2, 6.7 and 7.2 GHz. The red dashed lines have a slope of 2, which shows that the phase

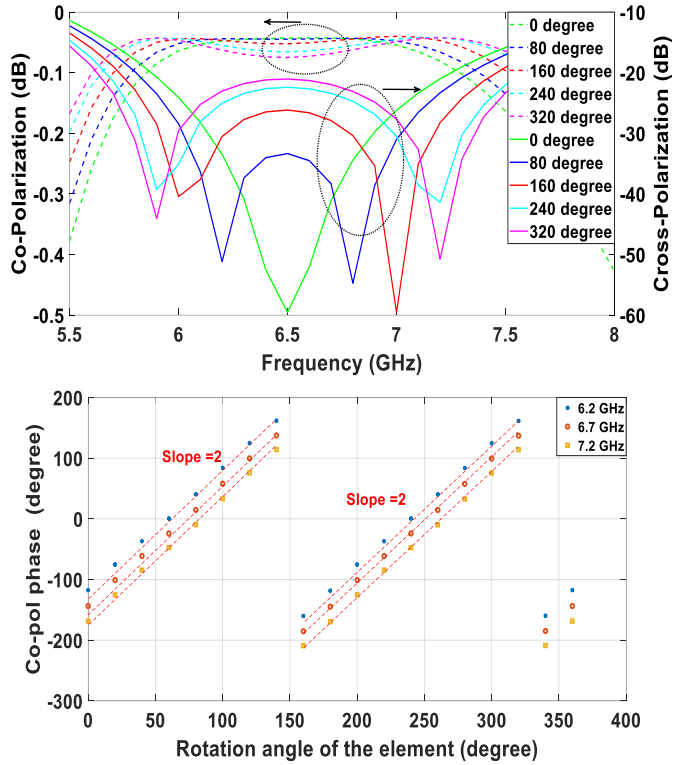

FIGURE 3. (a) Amplitude of co- and cross-polarized reflected waves for different rotation angles of the unit cell for normal incident angle (b) Co-polarization phase for different rotation angles of the unit cell at 6.2, 6.7 and 7.2GHz.

variation of Γ_{RR} is twice the rotation angle of the element, as expected.

The projected diameter of the dish in the xy plane is 24λ (102.7 cm), and the focal distance to diameter ratio (F/D) is 0.5. Given the small number of RSR elements, 32 and 4 of the 100 cells are, respectively, on the edges and corners of the array. Therefore, assuming identical far field patterns for all the elements of an infinite array will not give accurate beam synthesis results. To account for this, the embedded element factor of each RSR cell has been calculated, as explained in the next subsection. We have designed and fabricated the feed horn of the system, which is a dual-port septum-polarized horn antenna with the half power beamwidth (HPBW) of $36°$ and an axial ratio of less than 1 dB in the frequency range of 6-7.8 GHz. The beamwidth and horn positions were adjusted to properly illuminate the sub-reflectarray. Since the main reflector will change the sense of CP rotation, spillover of the horn fields around the subreflector will contribute to cross-polarization in the +z region.

B. BEAM SYNTHESIS ALGORITHM FOR THE PROPOSED SYSTEM

A beam synthesis algorithm was implemented to shape the far field pattern of the antenna expressed as a function of the direction cosines or (u, v) coordinates ($v = \sin\theta \sin\varphi$ and $u = \sin\theta \cos\varphi$, where θ and φ define the far field direction in the spherical coordinate system). For the chosen dish size, the antenna's main beam approximately covers the interval

This work is licensed under a Creative Commons Attribution-NonCommercial-NoDerivatives 4.0 License. For more information, see https://creativecommons.org/licenses/by-nc-nd/4

This article has been accepted for publication in IEEE Open Journal of Antennas and Propagation. This is the author's version which has not been fully edited and content may change prior to final publication. Citation information: DOI 10.1109/OJAP.2024.3477318

[-0.1, 0.1] in the *u* and *v* coordinates. Because the radiation intensity drops rapidly outside these intervals, it was decided to limit the beam synthesis to the range $[-0.3, 0.3]$ for both *u* and *v*. To realize beam synthesis by controlling the phases at the subreflector level, it is necessary to account for the reflection of each RSR element's fields on the main reflector. Because all elements have different positions in front of the dish, each element factor will be different. A simplified radiation source model that accounts for the specific element factors of all the array elements was proposed. In this model, the element factor $f_n(u,v)$ was defined as the contribution of the nth RSR element to the radiation pattern of the entire system. It consists of the fields scattered by the RSR element, which are then reflected by the parabolic dish and propagated to the far field. Therefore, the far-field pattern $F(u,v)$ is a weighted sum of all the element factors and is given by

$$F(u,v) = \sum_{n=1}^{N} a_n f_n(u,v) + F_{struc}(u,v) \tag{1}$$

In (1), $F_{struc}(u,v)$ is an antenna structure contribution to the far field pattern originating from scattering that is not directly affected by the excitation of the array elements. Functions $f_n(u,v)$ are complex element factors associated with the *N* elements of the RSR in the far field of the dish.

The a_n coefficients are associated with each RSR element. Their magnitudes are determined by the incident illumination from the horn on the nth element, and their phases, φ_n, can be controlled by element rotation. In the reference case used in the calibration process (see step 1a below), all φ_n values are considered to be zero. Therefore, φ_n is the difference between the phase of element *n* and the phase of element *n* in the reference state used in the calibration. In this state, the rotation angles of the unit cells are adjusted to generate a narrow beam in the far field of the reflector, for instance by having near-field focusing of the rays reflected by the RSR at the focal point of the dish. These rotations were determined by assuming identical behaviors for all unit cells (i.e., as in an infinite array).

The following steps were used to determine the functions $f_n(u,v)$ and $F_{struc}(u,v)$ using simulations of the antenna system, and (1) was used to synthesize the desired radiation patterns. It is assumed that the structural scattering term does not depend on the phase settings of the RSR elements; therefore, the two terms in (1) can be treated independently. For these simulations, a hybrid "MoM-PO" approach was used in which the feed horn and RSR were treated with the method of moments (MoM), while the main reflector was modeled using physical optics (PO). The FEKO simulation tool from Altair was used in this study.

1. Determination of $F_{struc}(u,v)$

a. With the RSR in the reference state, the pattern F^+ is calculated by simulating the entire system. This pattern corresponds to the following:

$$F^+(u,v) = \sum |a_n| e^{j\varphi_n} f_n(u,v) + F_{struc}(u,v) \tag{2}$$

For this reference case, we consider that the phases of all coefficients a_n are zero, that is, $\{\varphi_n\} = 0$. Therefore, we have

$$F^+(u,v) = \sum |a_n| f_n(u,v) + F_{struc}(u,v) \tag{3}$$

b. All the array elements are rotated by 90º in the same sense of rotation. This adds a phase of 180º to all a_n coefficients. In this case, the simulated pattern corresponds to

$$F^-(u,v) = \sum -|a_n| f_n(u,v) + F_{struc}(u,v) \tag{4}$$

c. Extract $F_{struc}(u,v)$ with

$$F_{struc}(u,v) = \frac{F^+ + F^-}{2} \tag{5}$$

Using this procedure, it was found that $|F_{struc}(u,v)|$ is 20 dB or more below $|F(u,v)|$ in the whole (u,v) range of interest. The structural scattering is therefore small compared to the RSR elements scattering.

2. Determination of the element patterns $f_n(u,v)$ for the N elements

a. Use the same setting as in Part 1a (i.e., $\{\varphi_n\} = 0$), except for the element number k. Rotate the element k by 90º. This effectively changes the phase of the kth element by 180º, thereby changing the sign of a_k. Using (1) we obtain

$$F_k(u,v) = \sum_{n \neq k} |a_n| f_n(u,v) - |a_k| f_k(u,v) + F_{struc}(u,v) \tag{6}$$

b. Based on the result of step 2a, and assuming that the magnitude of a_k is known, the element pattern associated with the kth unit cell can be obtained as

$$f_k(u,v) = \frac{F^+ - F_k}{2|a_k|} \tag{7}$$

The magnitude of a_k was obtained from the intensity of the horn illumination on element *k* in the desired polarization. This can be obtained by simulating the horn without the RSR and sampling the field amplitude of the horn at the location of element *k*, which corresponds to $|a_k|$.

This work is licensed under a Creative Commons Attribution-NonCommercial-NoDerivatives 4.0 License. For more information, see https://creativecommons.org/licenses/by-nc-nd/4

This article has been accepted for publication in IEEE Open Journal of Antennas and Propagation. This is the author's version which has not been fully edited and content may change prior to final publication. Citation information: DOI 10.1109/OJAP.2024.3477318

c. Repeat steps 2a and 2b for the N elements of the RSR. This yields the set of element patterns that can then be used in (1).

These element patterns correspond to the far field of the elements embedded in the entire system (horn, RSR, and dish). As implied by (7), 100 simulations of the whole system (horn, RSR, and dish) situated at the same physical location are necessary to obtain all the f_k's. As a result, there is no need for the usual path length factors $\exp(j\beta \mathbf{r}_k' \bullet \hat{\mathbf{r}})$ in the sum of (2). The path length factors are implicitly included in the element factors f_k.

3. Use an optimization algorithm to find the set of phases $\{\varphi_n\}$ to be applied to coefficients a_n to generate a desired far field pattern $F_d(u,v)$. Mean-square error (MSE) based only on the magnitude of the normalized patterns is first used:

$$MSE = \sum_{u,v} \left\| F_{d,normalized}(u,v) \right| - \left| F_{normalized}(u,v) \right\|^2 / P \tag{8}$$

where $F_{d,normalized}$ denotes the normalized desired pattern and $F_{normalized}$ denotes the normalized optimized pattern at the current iteration of the algorithm, and P denotes the number of sampling points in the (u,v) space.

The non-normalized pattern (1) can be rewritten as

$$F(u,v) = F_{struc}(u,v) + \sum_{n=1}^{N} \left| a_n \right| e^{j\varphi_n} f_n(u,v) \tag{9}$$

Altogether, N+2 simulations of the antenna are required to obtain the N element patterns, F^+, and F_{struct}, regardless of the number of iterations in the iterative beam synthesis process. During the iterative process, the sum in (8) is calculated over P selected points in the uv plane. For all the examples shown in this work, 256 sample points equally spaced in the range $(u,v) = ([-0.3, 0.3], [-0.3, 0.3])$ were used. This range was selected based on the geometry of the system and the wavelength. It covers the main beam of the focused beam and allows the demonstration of efficient beam shaping. In addition, the F_{struc} term was not considered in the beam synthesis procedure because it has an insignificant amplitude level compared to F^+.

The simulated and normalized reference radiation pattern of the dual-reflector antenna, F^+, are shown in Fig. 4 in the reference state, in which the feed horn beam reflected by the RSR is focused at the focal point of the dish. The reference rotations of the elements were adjusted using the standard path equalization RSR formula. The focal point was located between the RSR and dish, as in a Gregorian reflector system. For comparison, Fig. 4 also shows the pattern without the RSR, when the feed horn directly illuminated the dish. In this case, the beamwidth in the u and v coordinates is 2.5 times smaller. Using the RSR to shape the antenna pattern will clearly lead to a wider beam, with reduced aperture efficiency and higher sidelobes.

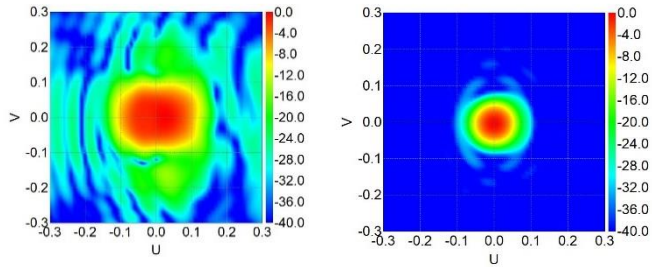

FIGURE 4. Normalized reference pattern in the *uv* plane (right-hand circular polarization, scale in dB). Left: structure in Fig. 1 with RSR, applying near-field focusing on the focal point of the dish. Right: no RSR, with the horn phase center at the focal point of the dish.

C. MODIFICATION TO THE ALGORITHM BY FORCING A CONTINUOUS PHASE DISTRIBUTION

The synthesis method described in Section IIB was applied using numerical examples for various beam shapes. Although the agreement of the calculated normalized patterns F with the desired patterns F_d was good and the MSE converged to stable and low values, the hybrid MoM-PO simulations of the antennas with the optimized sets of phase $\{\varphi_n\}$ led to poor agreement and distorted patterns. In [17], it was conjectured that these poor results are caused by the penalty function (8), which forces only the fitting of the desired and obtained patterns, without any constraint on the phase distribution over the array. The optimized phases exhibited rapidly varying distributions in the RSR. In the simplified model embodied in (1), the mutual interactions between a finite number of unit cells are considered more accurately when the phase distribution is close to the reference distribution. To obtain a more similar behavior of the model and the real RSR, one strategy could be to force the real RSR to have less abrupt variations in the distribution of the φ_n values. In [17], an approach to minimize abrupt phase variations between adjacent cells was proposed.

Based on this conjecture, the optimization algorithm should have two objectives: 1. minimizing the differences between the normalized synthesized and desired patterns and 2. maximizing the smoothness of the φ_n distribution in the RSR. The penalty function in (8) only considers the first objective. When calculating a metric for phase smoothness, one must be careful with the inevitable 2π discontinuities that occur in the phase distributions. These numerical transitions do not physically correspond to phase discontinuities. To avoid this difficulty, we chose to force smoothness of the complex quantity $\exp(j\varphi_n)$ instead of φ_n.

This work is licensed under a Creative Commons Attribution-NonCommercial-NoDerivatives 4.0 License. For more information, see https://creativecommons.org/licenses/by-nc-nd/4

This article has been accepted for publication in IEEE Open Journal of Antennas and Propagation. This is the author's version which has not been fully edited and content may change prior to final publication. Citation information: DOI 10.1109/OJAP.2024.3477318

To allow the desired beam steering, we do not want to penalize the phase gradient but rather the fast variations in the phase gradient. Such variations occur at points in the phase distribution (referred to as phase singularities) that are significantly different from the phases at the surrounding points. A continuous phase gradient with no singularities indicates that the gradient has no divergence. Thus, the aim is to minimize the divergence of the phase gradient, that is, the Laplacian of the phase distribution:

$$\nabla \bullet \nabla \varphi = \nabla^2 \varphi \tag{10}$$

or the complex exponential

$$\nabla^2 \exp(j\varphi) \tag{11}$$

The Laplacian of the discrete distribution at element (i, j) was approximated numerically by employing finite differences using (12) [16].

$$\begin{aligned}\nabla^2 \exp(j\varphi_{i,j}) \approx \exp(j\varphi_{i,j}) - \frac{1}{4}(\exp(j\varphi_{i-1,j}) + \exp(j\varphi_{i+1,j}) \\ + \exp(j\varphi_{i,j-1}) + \exp(j\varphi_{i,j-1}))\end{aligned} \tag{12}$$

where $\varphi_{i,j}$ (corresponding to φ_n) is the phase applied to the unit cell at point n with coordinates (x_i, y_j). The new objective function to be minimized can then be written as:

$$\begin{aligned}OBJ = \sum_{u,v} \left\| F_{d,normalized}(u,v) \right| - \left| F_{normalized}(u,v) \right\|^2 / P \\ + \alpha \sum_{i,j} \left| \nabla^2 \exp(j\varphi_{i,j}) \right| / N\end{aligned} \tag{13}$$

Absolute values are used in the Laplacian because positive and negative Laplacians can partially cancel out when they are summed in (13), which would overestimate the smoothness of the phase distribution. Constant α is a real parameter to be tuned. Several numerical experiments were required to adjust α, starting with a low value and then increasing it progressively. The value of α should not be too large because it may "over-smooth" the phase and decrease the relative weight of the first term in the MSE forcing pattern fitness.

D. PARTICLE SWARM OPTIMIZATION (PSO) APPLIED TO SUB-REFLECTARRAY PHASE SYNTHESIS

This section introduces the PSO algorithm as an optimization approach to determine the appropriate phase distribution on the RSR for synthesizing the beam of a dual-reflector antenna. PSO is an iterative algorithm based on the search of birds hunting for food [24]. The algorithm aims to minimize *OBJ*, as defined in (13). In our case, the algorithm stopped when a pre-defined iteration number was reached. The population number, that is, the number of "particles," is a primary parameter to be defined for solving the algorithm. Each particle *i* represents a potential solution. A solution consists of a set of phase shifts applied by the RSR elements. In this work, we consider an RSR of 10 × 10 cells on a square lattice. A velocity parameter is used to control the moving track of each particle during the search process of the algorithm. Velocity (***v***) and position (***x***) are vectors that define the state of each particle in the algorithm. Both vectors have 100 elements, which are updated at iteration $m+1$, as follows:

$$\boldsymbol{v}_i^{m+1} = \omega \cdot \boldsymbol{v}_i^m + c_1 \cdot \boldsymbol{r}_1 \odot (\boldsymbol{p}_i^m - \boldsymbol{x}_i^m) + c_2 \cdot \boldsymbol{r}_2 \odot (\boldsymbol{g}^m - \boldsymbol{x}_i^m) \tag{14}$$

$$\boldsymbol{x}_i^{m+1} = \boldsymbol{v}_i^{m+1} + \boldsymbol{x}_i^m . \tag{15}$$

In (14), ω is the inertia weight, which has a scalar value, and the scalars c_1 and c_2 are the acceleration coefficients, whereas $\boldsymbol{r}_1$ and $\boldsymbol{r}_2$ are random vectors of 100 real numbers in the range [0,1], which are updated in each iteration. The circled dot symbol corresponds to the Hadamard product. The position and velocity of the ith particle were given by $\boldsymbol{x}_i = (x_{i1}, x_{i2}, ..., x_{i100})^T$ and $\boldsymbol{v}_i = (v_{i1}, v_{i2}, ..., v_{i100})^T$, respectively. In (14), $\boldsymbol{p}_i$, called the personal best position, is the position vector that gives the best cost of the ith particle over all previous iterations, while $\boldsymbol{g}$ is the global best position vector with the best cost value among all particles over all previous iterations.

On the right-hand side of (14), the first term is related to the velocities of the particles in the previous iteration, the second term is associated with each particle's behavior, and the third term is a "social" contribution, which expresses the cooperation among the particles [25, 26].

The algorithm begins by assigning100 arbitrary values to the position vector for all the particles (corresponding to $\{\varphi_{i,j}\}$) and assigning zeros to the velocity vector. The two best positions, including the parameters of the global and personal best solutions, update the particles as potential solutions. The set of 100 phases in each particle is updated in each iteration. After the last iteration, the optimized phase distribution of the particle with the best global cost was used to calculate the far-field pattern. As this is a minimization problem, the global best cost is initialized to a very large value. A flowchart of the PSO algorithm for a pre-defined iteration number is shown in [23].

III. BEAM SHAPING EXAMPLES

The beam shaping property of the antenna using the proposed algorithm was investigated. For this purpose, we considered three tapered Gaussian patterns defined by (16) as the desired beams. Table 2 lists the parameters of the PSO-based algorithm used to synthesize these patterns. To evaluate *OBJ* in a reasonable computation time, each pattern is sampled at 256 sample points in the range $[-0.3, 0.3]$, for *u* and *v*, which cover the main beam and near side lobes.

This work is licensed under a Creative Commons Attribution-NonCommercial-NoDerivatives 4.0 License. For more information, see https://creativecommons.org/licenses/by-nc-nd/4

This article has been accepted for publication in IEEE Open Journal of Antennas and Propagation. This is the author's version which has not been fully edited and content may change prior to final publication. Citation information: DOI 10.1109/OJAP.2024.3477318

$$F_d(u,v) = e^{-\left(u^2/\left(2\sigma_u^2\right)+v^2/\left(2\sigma_v^2\right)\right)} \tag{16}$$

A large number of iterations was performed to ensure that *OBJ* stabilized before the end of the process. All the results shown are for a frequency of 7 GHz. For each example, the performance of the algorithm is illustrated by comparing the normalized pattern computed with (9) using the phases obtained by PSO with the normalized pattern obtained with the hybrid MoM-PO solution using the same phases. Fig. 5 shows the convergence of *OBJ* for the first example in Table 2. It can be seen that *OBJ* converged to a low value after only a few hundred iterations and that the first and second terms stabilized at nearly the same number of iterations for the chosen value of parameter α.

TABLE 2. ALGORITHM PARAMETERS FOR SHAPING THREE DESIRED BEAMS

Desired pattern		Population number	Iteration number	α	*OBJ*
1	σ_v =0.105 σ_u =0.075	2000	3000	5e-3	0.00133
2	σ_v =0.075 σ_u =0.075	2000	3000	5e-3	0.00108
3	σ_v =0.045 σ_u =0.075	2000	3000	5e-3	0.0026

The results for the Gaussian pattern with σ_v =0.105 and σ_u =0.075 are shown in the first row of Fig. 6. Fig. 6(a) shows the desired beam sampled at 256 (*u*,*v*) points. Figs. 6(b) and 6(c) show, respectively, the pattern calculated with (9) and the distribution of φ_n on the RSR obtained from PSO, using $\{\varphi_{i,j}\}$ of the last iteration. Fig. 6(d) shows the radiation pattern in the *uv* plane obtained by MoM-PO, after applying the phase distribution in Fig. 6(c) to the subreflector elements. The -10 dB beamwidths for the patterns in subfigures (b) and (d) are reported in Table 3 for the three test cases. For the first example, the beamwidths predicted by the PSO optimization along the $u = 0$ and $v = 0$ planes give $\Delta v = 0.32$ and $\Delta u = 0.22$, respectively, whereas the MoM-PO simulated pattern gives $\Delta v = 0.36$ and $\Delta u = 0.22$. Therefore, the optimized and simulated results agree well with those of the desired Gaussian pattern. For the second example, the results with σ_v =0.075 and σ_u =0.075 are shown in the second row of Fig. 6. The -10 dB beamwidths predicted by PSO (Fig. 6(b)) are $\Delta v = 0.22$ and $\Delta u = 0.22$, whereas the MoM-PO simulation of the antenna (Fig. 6(d)) gives $\Delta v = 0.23$ and $\Delta u = 0.22$. Again, a very good agreement was observed.

For the third example, we consider σ_v =0.0045 and σ_u =0.075; the results are shown in the third row of Fig. 6. PSO predicted $\Delta v = 0.15$ and $\Delta u = 0.21$ for -10 dB beamwidths, while the MoM-PO simulation provided $\Delta v = 0.15$ and $\Delta u = 0.21$. As in the desired pattern, both figures have a narrower beam for the *u*=0 cut than for the *v*=0 cut.

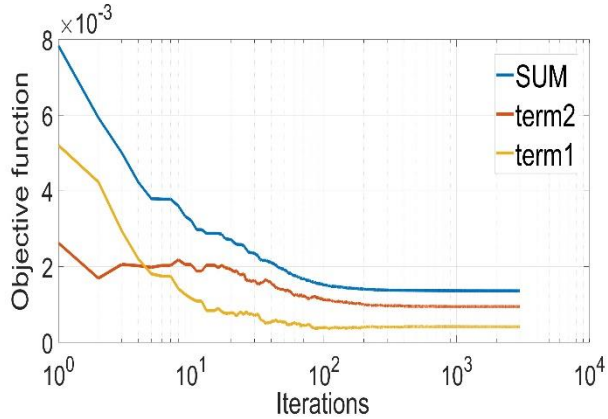

FIGURE 5. Total, first and second terms of objective function (13) vs. iteration number for σ_v = 0.105 and σ_u = 0.075, with α = 0.005.

TABLE 3. -10 DB beamwidth of examples in Fig. 6

Centered Gaussian pattern	Method	BW (-10dB) along the *v* axis	BW (-10dB) along the *u* axis
Reference pattern	Pattern simulated by PO-MoM	$\Delta v = 0.175$ 10 ^{o}	$\Delta u = 0.225$ 13 ^{o}
σ_v =0.105 σ_u =0.075	Desired Gaussian pattern	$\Delta v = 0.32$ 18.6 ^{o}	$\Delta u = 0.22$ 12.7 ^{o}
	Pattern optimized by PSO	$\Delta v = 0.32$ 18.6 ^{o}	$\Delta u = 0.22$ 12.7 ^{o}
	Pattern simulated by PO-MoM	$\Delta v = 0.36$ 21.1 ^{o}	$\Delta u = 0.22$ 12.7 ^{o}
σ_v =0.075 σ_u =0.075	Desired Gaussian pattern	$\Delta v = 0.22$ 12.7 ^{o}	$\Delta u = 0.22$ 12.7 ^{o}
	Pattern optimized by PSO	$\Delta v = 0.22$ 12.7 ^{o}	$\Delta u = 0.22$ 12.7 ^{o}
	Pattern simulated by PO-MoM	$\Delta v = 0.23$ 13.29 ^{o}	$\Delta u = 0.22$ 12.7 ^{o}
σ_v =0.045 σ_u =0.075	Desired Gaussian pattern	$\Delta v = 0.13$ 7.46 ^{o}	$\Delta u = 0.22$ 12.7 ^{o}
	Pattern optimized by PSO	$\Delta v = 0.15$ 8.6^o	$\Delta u = 0.21$ 12.12 ^{o}
	Pattern simulated by PO-MoM	$\Delta v = 0.15$ 8.6 ^{o}	$\Delta u = 0.21$ 12.12 ^{o}

This work is licensed under a Creative Commons Attribution-NonCommercial-NoDerivatives 4.0 License. For more information, see https://creativecommons.org/licenses/by-nc-nd/4

This article has been accepted for publication in IEEE Open Journal of Antennas and Propagation. This is the author's version which has not been fully edited and content may change prior to final publication. Citation information: DOI 10.1109/OJAP.2024.3477318

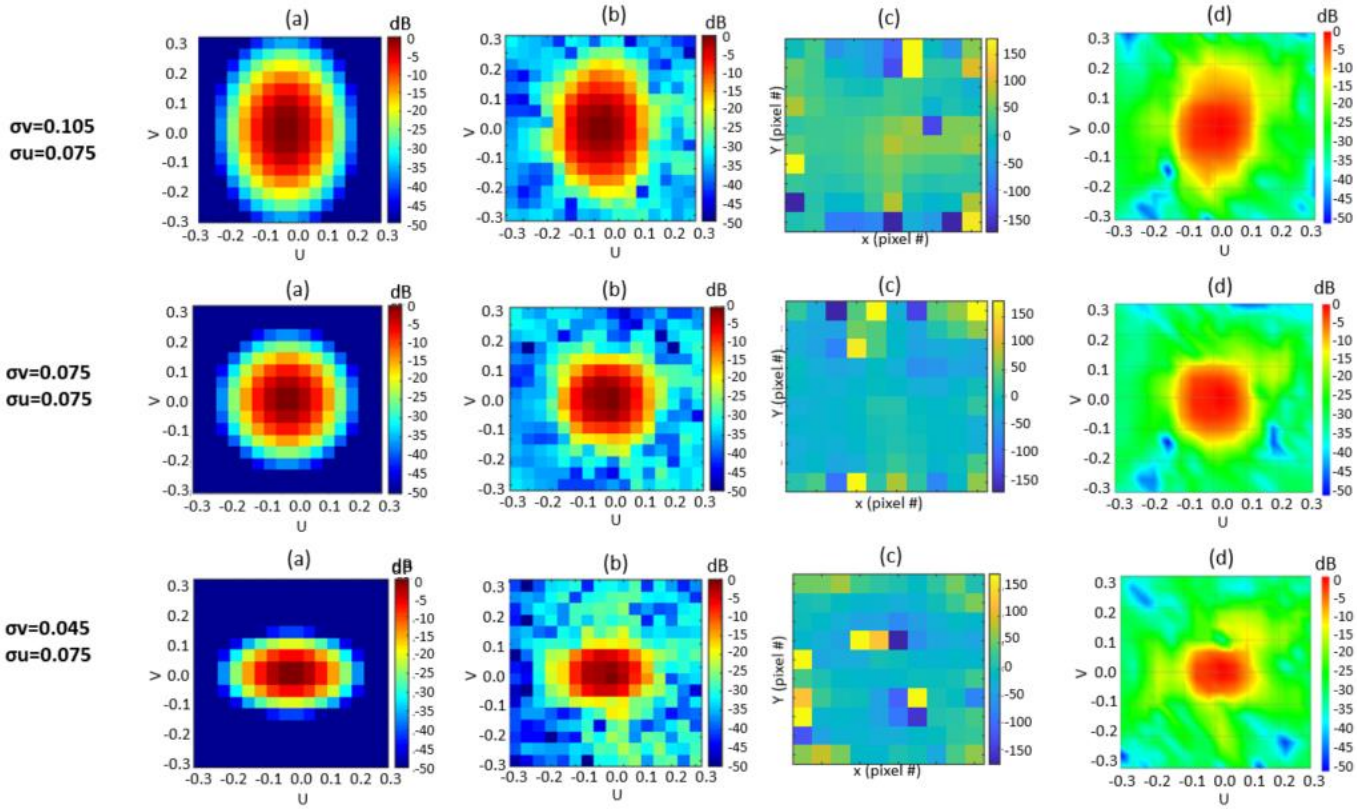

FIGURE 6. **(a) Sampled centered Gaussian patterns with σ_v =0.105 and σ_u =0.075, σ_v =0.075 and σ_u =0.075, and σ_v =0.045 and σ_u =0.075. (b) Normalized amplitude of $F(u,v)$ optimized by PSO. (c) Distribution of φ_n in degrees on the reflectarray for the optimized pattern. (d) Normalized amplitude of $F(u,v)$ simulated with MoM-PO using the phase distribution in (c).**

IV. EXPERIMENTAL VALIDATION

A. DESCRIPTION OF THE EXPERIMENTAL SETUP

This section aims to experimentally demonstrate the capability of the proposed beam synthesis method for dual-reflector antennas. For this purpose, the structure shown in Fig. 7 was used, which is similar to the dual-reflector antennas shown in Fig. 1. Both configurations have the same RSR size and horn. However, the dish size of the measurement setup in Fig. 7 is smaller owing to the limited size of the quiet zone of the compact antenna test range (CATR) available to the authors. The major and minor axes of the projected aperture of the elliptically shaped dish are 65 cm (15.18λ) and 43.3 cm (10.11λ), respectively, with a focal distance of 49.2 cm (11.14λ at the design frequency of 7 GHz). Owing to the smaller dimensions of the reflector, the displacement of the illuminated region on the reflector caused by variations in the phase distribution on the subreflector is more likely to cause spillover and should therefore be limited. Nevertheless, it is possible to observe variations in the beamwidth created by the beam synthesis. Fig. 8 shows the CATR measurement setup used to measure the far-field cuts along the *v* and *u* axes.

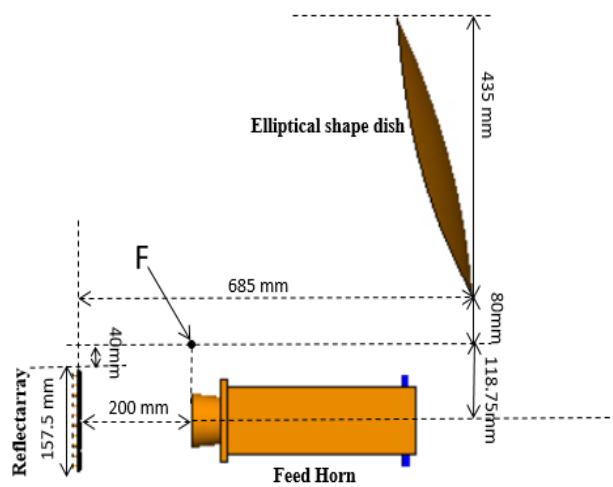

FIGURE 7. **Dual-reflector antenna for the measurement setup, including a horn, a reconfigurable sub-reflectarray, and a solid parabolic dish. The clearance between the top edge of the reflectarray and the bottom edge of the main reflector is 120 mm, and the distance between the reflectarray and the horn is 200 mm, with an illumination of -4.2 dB on the edges of the reflectarray.**

This work is licensed under a Creative Commons Attribution-NonCommercial-NoDerivatives 4.0 License. For more information, see https://creativecommons.org/licenses/by-nc-nd/4

This article has been accepted for publication in IEEE Open Journal of Antennas and Propagation. This is the author's version which has not been fully edited and content may change prior to final publication. Citation information: DOI 10.1109/OJAP.2024.3477318

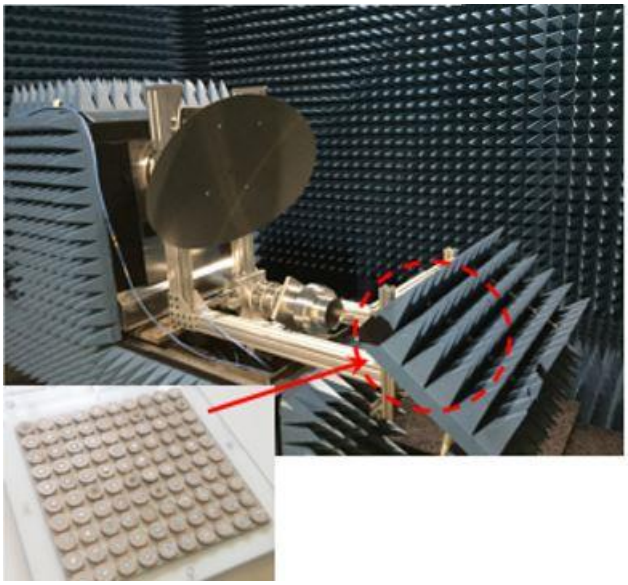

FIGURE 8. Setup for measuring the pattern cuts along the *u* and *v* axes.

B. EXPERIMENTAL RESULTS

A centered tapered Gaussian pattern was used as the desired beam. Before applying the beam synthesis algorithm, a new set of element factors of the 100-element RSR (i.e., the functions f_k of (7)) must be generated for the dual-reflector structure in Fig. 7, that is, with the smaller elliptical dish. Once this step is completed, beam synthesis is performed and the obtained phases are applied to the RSR elements in the experimental antenna. Again, all phases are relative to the phases of a reference pattern, in which the elements are adjusted so that the beam reflected by the RSR is focused at the focal point of the dish. Fig. 9 shows the co-polarization reference pattern of the system in the far field of the antenna, as calculated by MoM-PO. The elliptical dish model is used in the beam synthesis steps presented in Section II and in the far field computations.

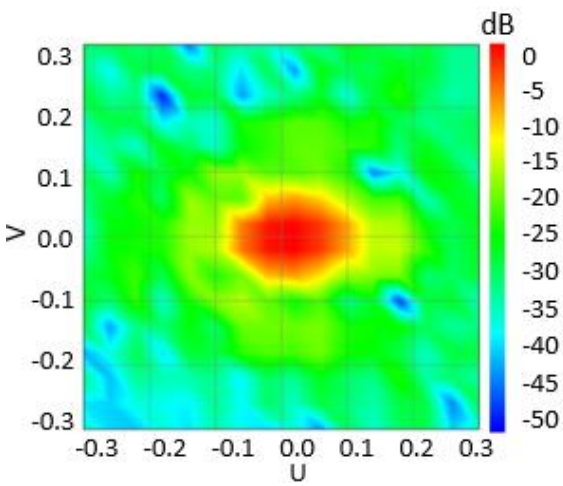

FIGURE 9. Reference radiation pattern of the structure in Fig. 7.

As an illustrative example, the centered Gaussian pattern with σ_v =0.09 and σ_u =0.06, as shown in Fig. 10(a), is defined as the desired beam. The PSO algorithm with a population number of 5000 and α =5e-3 yields an *OBJ* value of 0.0032 after 1000 iterations. These parameters were determined through several numerical experiments. Figs. 10(b) and 10(c) show the pattern in the *uv* plane and the φ_n phase distribution on the RSR obtained from PSO, respectively. Fig. 10(d) shows the radiation pattern in the *uv* plane of the dish calculated by MoM-PO after applying the optimized phase distribution. As desired, the synthesized pattern in Fig. 10(d) had a wider beam than the reference pattern in Fig. 9 along the *u*=0 axis. Cuts along the *u* and *v* axes of the patterns in Figs. 9 and 10(d) are shown in Figs. 11(a) and 11(b), respectively. Each figure includes the measured and simulated cuts for the reference pattern and the desired Gaussian patterns, together with the theoretical desired patterns. Both the simulation and measurement results show the capability to widen the beam along one axis while keeping the width almost constant along the other axis. The -10 dB beamwidths are reported in Table 4. For the *u*=0 cut, the desired, simulated, and measured Gaussian patterns have nearly similar beamwidths, which are larger than those of the reference case. However, in the *v*=0 cut, the beamwidths of the desired, simulated, and measured Gaussian patterns were similar to that of the reference beam. For the proposed experimental setup, the optimization algorithm works with a reduced solution space owing to the limited dish size. This effect is observed in Fig. 12 by comparing the current distributions on the dish for the structures in Fig. 1 and Fig. 7, when synthesizing the beam for centered Gaussian patterns. A few reasons could explain the differences between the measured and MoM-PO

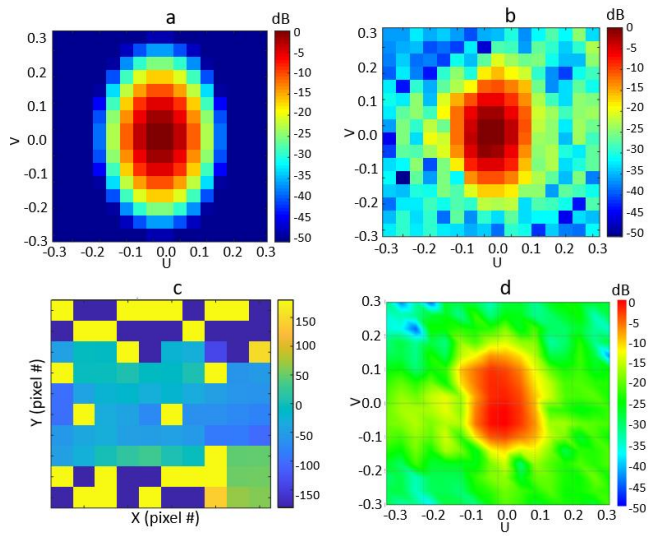

FIGURE 10. (a) Centered Gaussian pattern with σ_v =0.09 and σ_v =0.06. (b) Normalized amplitude of the optimized pattern by PSO. (c) Distribution of φ_n in degrees on the reflectarray for the optimized pattern. (d) Normalized co-polarization amplitude of the radiation pattern obtained by simulation of the antenna in FEKO using the phase distribution $\{\varphi_n\}$ in (c).

This work is licensed under a Creative Commons Attribution-NonCommercial-NoDerivatives 4.0 License. For more information, see https://creativecommons.org/licenses/by-nc-nd/4

This article has been accepted for publication in IEEE Open Journal of Antennas and Propagation. This is the author's version which has not been fully edited and content may change prior to final publication. Citation information: DOI 10.1109/OJAP.2024.3477318

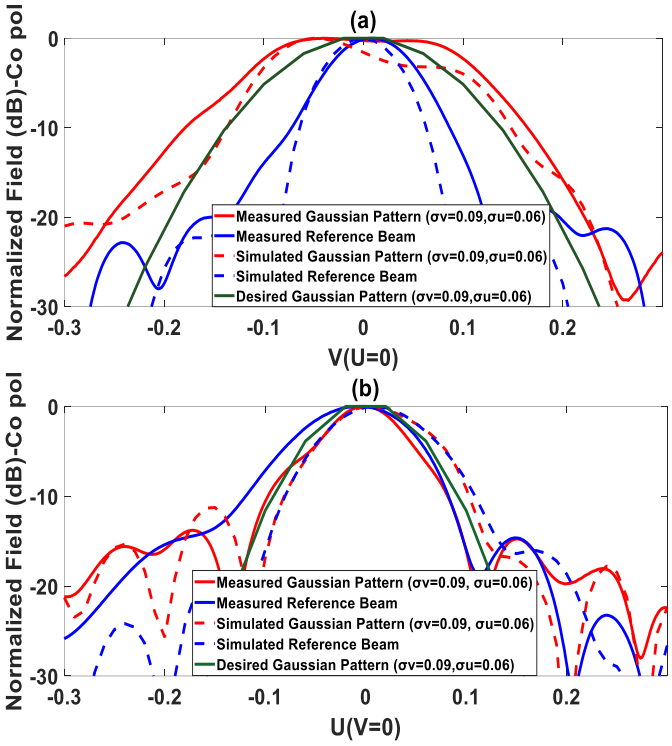

FIGURE 11. Cuts of the Gaussian pattern with σ_v =0.09 and σ_u =0.06. (a) Normalized co-polarization electric field along the *v* axis (*u*=0) for the reference beam (measured) and the synthesized beams (measured, simulated, and desired) for the Gaussian patterns. (b) Same cases but along the *u* axis (*v*=0).

simulated results. First, we used a: low-quality commercial reflector antenna that was cut to fit in the quiet zone of the CATR. Second, misalignments of the horn, sub-reflectarray and dish are possible.

TABLE 4. -10 dB BW of the reference and synthesized beams

Pattern	Method	BW (-10dB) along the v axis	BW (-10dB) along the u axis
Reference pattern	Pattern optimized by PSO	$\Delta v = 0.15$, 8.62º	$\Delta u = 0.2$, 11.53º
	Pattern simulated by PO-MoM	$\Delta v = 0.13$, 7.4º	$\Delta u = 0.19$, 10.9º
	Measurement	$\Delta v = 0.16$, 9.2º	$\Delta u = 0.2$, 11.5º
Gaussian pattern with σ_v =0.09 and σ_u =0.06	Desired Gaussian pattern	$\Delta v = 0.28$, 16.26º	$\Delta u = 0.2$, 11.53º
	Pattern optimized by PSO	$\Delta v = 0.3$, 17.45º	$\Delta u = 0.21$, 11.53º
	Pattern simulated by PO-MoM	$\Delta v = 0.28$, 16.0º	$\Delta u = 0.19$, 10.9º
	Measurement	$\Delta v = 0.34$, 19.6º	$\Delta u = 0.18$, 10.3º

Third, the simulations did not include the reflectarray mounting brackets; they were covered with absorbers during

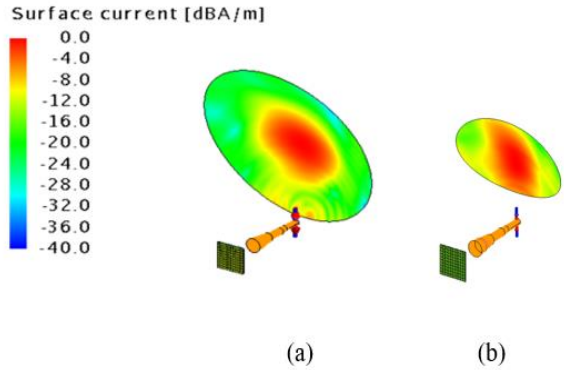

FIGURE 12. Current distribution on the dish obtained by simulation of the antenna in FEKO, using (a) the phase distribution $\{\varphi_n\}$ in Fig. 6(c) for the centered Gaussian pattern with σ_v =0.105 and σ_u =0.075 and (b) the phase distribution in Fig. 10(c) for the centered Gaussian pattern with σ_v =0.09 and σ_u =0.06.

the tests and these absorbers can cause some blockage that affects the patterns.

Fig. 13 shows the normalized reference and synthesized patterns along the *v* and *u* axes obtained from measurement. XPD levels of approximately 15 dB and 19 dB (AR of 1.5dB and 0.97dB) within the HPBW along the *v* and *u* axes were obtained, respectively, for the synthesized beam, while an XPD of approximately 25 dB (AR of 0.48dB) was obtained for the reference beam along both axes. The RHCP term is considered to be the co-polarization term, and LHCP is deemed to be the cross-polarization term. These XPD levels were higher than those of the unit cell (see Fig. 3). However, the optimization algorithm did not include X-pol and it did not calculate the element patterns for X-pol. It can be observed that for the case of the focused beam, the XPD level is better than that of the shaped beam. This was also the case in [16]. A comparison of different studies in which a sub-reflectarray is used for beam shaping is given in Table 5. To the best of our knowledge, this paper is the first to include an experimental demonstration with a reconfigurable sub-reflectarray. Accordingly, the number of array elements was significantly smaller. This study is also the first to consider circular polarization. Except for [5], it can be observed that aperture efficiency increases when the size of the subreflectarray increases, possibly due to less spillover losses.

V. CONCLUSION

The proposed approach for synthesizing beams in a dual-reflector system using RSR element factors was demonstrated through simulations and validated experimentally with smooth Gaussian patterns. It was shown that the proposed algorithm can control the beamwidth along the *v* and *u* axes. Good agreement was found between the beamwidths predicted by optimization and those obtained from the simulations. Owing to the limitations of the antenna test range, a smaller main reflector was used in the experiments, leading to stronger currents near the edge of the reflector (Fig. 12(b)). This led to

This work is licensed under a Creative Commons Attribution-NonCommercial-NoDerivatives 4.0 License. For more information, see https://creativecommons.org/licenses/by-nc-nd/4

This article has been accepted for publication in IEEE Open Journal of Antennas and Propagation. This is the author's version which has not been fully edited and content may change prior to final publication. Citation information: DOI 10.1109/OJAP.2024.3477318

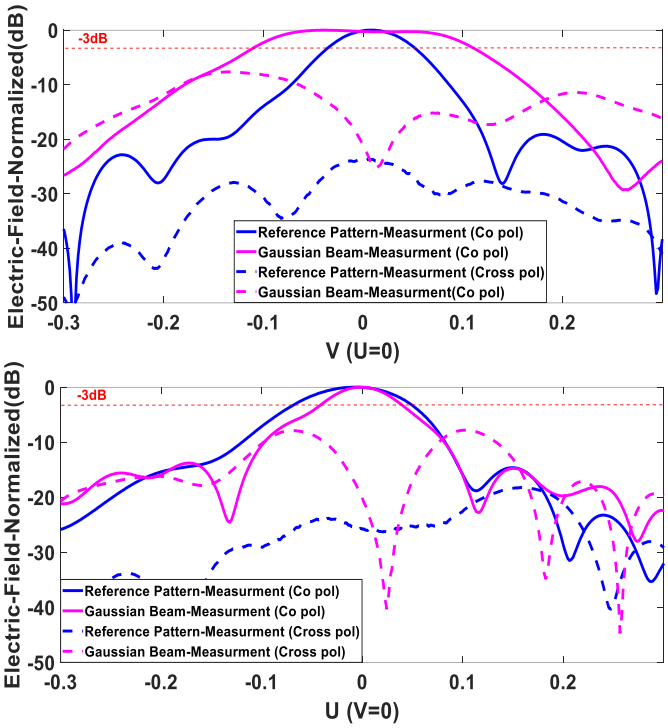

FIGURE 13. Normalized far-field of the reference beam (measured) and desired Gaussian beams with σ_v =0.09 and σ_u =0.06 cuts (measured): (a) along the *v* axis (*u*=0), (b) along the *u* axis (*v*=0)

more differences between the measured and predicted beamwidths, but the agreement for the -10 dB beamwidths was still within a few degrees (differences of 0.6º for the narrow width and 3.6º for the wider width). It is concluded that the limitation of the algorithm in terms of controlling the beamwidth, especially for narrow beams, can be improved by increasing the aperture size of the main reflector. In all test cases, with an RSR of only 100 elements, the addition of a penalty term in the PSO criterion to prevent abrupt variations in the phase settings was found to be essential. Applying this approach to an N-element RSR first requires N+2 simulations of the entire antenna system (one for each element, one for the structural scattering term, and one for the reference beam). A hybrid approach in which the RSR and feed horn were modeled with MoM and the main reflector was modeled with PO led to good results. Once this computation-intensive phase is performed, beam optimization is realized rapidly and efficiently.

REFERENCES

[1] M. M. Dehnavi and J.-J. Laurin, "Beam scanning dual reflector antenna with a circularly polarized reconfigurable reflectarray as subreflector," in *70th Int. Astron, Cong. (IAC 2019)*, Washington, DC, 2019.

[2] M. Arrebola, L. D. Haro, and J. A. Encinar, "Analysis of dual-reflector antennas with a reflectarray as subreflector," *IEEE Antennas and Propagation Magazine*, vol. 50, no. 6, pp. 39–51, Dec. 2008.

[3] C. Tienda, M. Arrebola, and J.A. Encinar, "Review article: Recent developments of reflectarray antennas in dual-reflector configurations," *International Journal of Antennas and Propagation*, vol. 2012, May. 2012.

[4] M. Arrebola, L. de Haro, J. A. Encinar and L. F. de la Fuente, "Contoured-Beam Gregorian Antenna with a Reflectarray as Subreflector," The Second European Conference on Antennas and Propagation, EuCAP 2007, Edinburgh, 2007, pp. 1-6, doi: 10.1049/ic.2007.0942

[5] M. Arrebola, E. Carrasco, and J. A. Encinar, "Beam scanning antenna using a reflectarray as sub-reflector," *Applied Computational Electromagnetics Society Journal*, vol. 26, no. 6, pp.473-483, June 2011.

[6] W. Hu et al., "94 GHz Dual-Reflector Antenna With Reflectarray Subreflector," IEEE Trans. Antennas Propagat, vol. 57, pp. 3043-3050, Oct. 2009.. Tienda, M. Arrebola, and J.A. Encinar, "Review article: Recent developments of reflectarray antennas in dual-reflector configurations," *International Journal of Antennas and Propagation*, vol. 2012, May. 2012.

[7] O. M. Bucci, G. Franceschetti, G. Mazzarella, and G. Panariello, "Intersection approach to array pattern synthesis," in *IEE Proceedings H (Microwaves, Antennas, and Propagation)*, vol. 137, no. 6, pp. 349–357, Dec. 1990.

[8] D. R. Prado, M. Arrebola, M. R. Pino, and F. Las-Heras, "Improved reflectarray phase-only synthesis using the generalized intersection

TABLE 5. Comparison of systems implementing beam shaping with a sub-reflectarray

	[2]	[4]	[5]	[6]	[22]	This work
Beam shaping	No	Yes	No	No	No	Yes
Reconfigurable sub-Reflectarray element	No	No	Yes (simulated)	No	No	Yes (Fabricated)
Polarization	Linear	Linear	Linear	Linear	Linear	Circular
Experimental proof of concept	No	No	No	Yes	Yes	Yes
Reflectarray size (lambda^2)	20 x 20	22.3 x 22.3	11.7 x 10.75	8.8 x 8.8	1.63 x 1.43	3.65 x 3.65
Reflectarray shape	Square	Square	elliptical	Square	Square	Square
Number of sub-Reflectarray elements	1600	2601	420	784	25	100
Main reflector size (lambda^2)	2803	2803	1168	1110	14.7	120.5
Realized Gain (dBi)	43	43	35	38.7	15.8	26.9
Frequency (GHz)	11.95	11.95	11.7	94	2.45	7
Aperture efficiency	56%	56%	21%	53%	20%	32%

This work is licensed under a Creative Commons Attribution-NonCommercial-NoDerivatives 4.0 License. For more information, see https://creativecommons.org/licenses/by-nc-nd/4

This article has been accepted for publication in IEEE Open Journal of Antennas and Propagation. This is the author's version which has not been fully edited and content may change prior to final publication. Citation information: DOI 10.1109/OJAP.2024.3477318

approach with dielectric frame and first principle of equivalence," *International Journal of Antennas and Propagation*, May 2017.

[9] W. Stutzman and E. Coffey, "Radiation pattern synthesis of planar antennas using the iterative sampling method," in *IEEE Transactions on Antennas and Propagation*, vol. 23, no. 6, pp. 764–769, Nov. 1975.

[10] E. R. Schlosser, S. M. Tolfo, and M. V. T. Heckler, "Particle swarm optimization for antenna arrays synthesis," *2015 SBMO/IEEE MTT-S International Microwave and Optoelectronics Conference (IMOC)*, Porto de Galinhas, Brazil, 2015.

[11] L. A. Greda, A. Winterstein, D. L. Lemes, and M. V. T. Heckler, "Beamsteering and beamshaping using a linear antenna array based on particle swarm optimization," *IEEE Access*, vol. 7, pp. 141562–141573, 2019.

[12] A. K. Bhattacharyya, "Projection matrix method for shaped beam synthesis in phased arrays and reflectors," *IEEE Transactions on Antennas and Propagation*, vol. 55, no. 3, pp. 675–683, Mar. 2007.

[13] Zornoza, J. Agustín, and Jose A. Encinar., "Efficient phase-only synthesis of contoured-beam patterns for very large reflectarrays," *International Journal of RF and Microwave Computer-Aided Engineering* , vol. 14, no. 5, pp. 415–423, 2004.

[14] M.A. Zaman *et al*., "Phased array synthesis using modified particle swarm optimization," *Journal of Engineering Science & Technology Review*, vol. 4, no. 1, pp 68-73, Jan. 2011.

[15] M. M. Dehnavi, "Beam Shaping and Beam Scanning of C-band Circularly Polarized Dual Reflector Antenna Using Reconfigurable Subreflector," Ph.D. dissertation, Dept. Elect. Eng., Polytechnique Mtl., Montreal, Canada, 2021.

[16] X. Yang *et al*., "A broadband high-efficiency reconfigurable reflectarray antenna using mechanically rotational elements," *IEEE Transactions on Antennas and Propagation*, vol. 65, no. 8, pp. 3959–3966, 2017.

[17] M. M. Dehnavi and J.-J. Laurin, "Beam synthesis of a C-band circularly polarized dual-reflector antenna using a reconfigurable subreflector," in *2021 XXXIVth Gen. Ass. and Sci. Symp Int. Union of Rad. Sci.(URSI GASS)*, Rome, Italy, Sept. 2021.

[18] N. Zhang *et al*., "A Dual-Polarized Reconfigurable Reflectarray Antenna Based on Dual-Channel Programmable Metasurface," in *IEEE Transactions on Antennas and Propagation*, vol. 70, no. 9, pp. 7403-7412, Sept. 2022, doi: 10.1109/TAP.2022.3165872.

[19] H. Zhang, X. Chen, Z. Wang, Y. Ge and J. Pu, "A 1-Bit Electronically Reconfigurable Reflectarray Antenna in X Band," in *IEEE Access*, vol. 7, pp. 66567-66575, 2019, doi: 10.1109/ACCESS.2019.2918231

[20] I. -J. Nam, S. Lee and D. Kim, "Miniaturized Beam Reconfigurable Reflectarray Antenna With Wide 3-D Beam Coverage," in *IEEE Transactions on Antennas and Propagation*, vol. 70, no. 4, pp. 2613-2622, April 2022, doi: 10.1109/TAP.2021.3083732.

[21] X. Li, H. Sato, H. Fujikake and Q. Chen, "Development of Two-Dimensional Steerable Reflectarray With Liquid Crystal for Reconfigurable Intelligent Surface Applications," in *IEEE Transactions on Antennas and Propagation*, vol. 72, no. 3, pp. 2108-2123, March 2024, doi: 10.1109/TAP.2024.3354054.

[22] Kulkarni, Shashank S., et al. "Planar metasurface sub-reflector based dual-reflector antenna for multi-directional beaming." AEU-International Journal of Electronics and Communications 164 (2023): 154621.

[23] M. M. Dehnavi and. J.-J. Laurin, "C-band circularly polarized reconfigurable reflectarray unit cells," in *2017 XXXIInd Gen. Ass. and Sci. Symp. of Int. Union of Rad. Sci. (URSI GASS)*, Montreal, Canada, 2017.

[24] B. Kadri and M. Brahimi, "Patterns antennas arrays synthesis based on adaptive particle swarm optimization and genetic algorithms," *International Journal of Computer Science Issues (IJCSI)*, vol. 10, no. 1, p. 21, 2013.

[25] T. B. Chen, Y. B. Chen, Y. C. Jiao, and E. S. Zhang, "Synthesis of antenna array using particle swarm optimization," in *2005 Asia-Pacific Microwave Conference Proceedings*, Suzhou, China, 2005.

Y. Rahmat-Samii, D. Gies, and J. Robinson, "Particle swarm optimization (PSO): A novel paradigm for antenna designs," *URSI Radio Science Bulletin*, vol. 2003, no. 306, pp. 14–22, Sept. 2003.

This work is licensed under a Creative Commons Attribution-NonCommercial-NoDerivatives 4.0 License. For more information, see https://creativecommons.org/licenses/by-nc-nd/4

This article has been accepted for publication in IEEE Open Journal of Antennas and Propagation. This is the author's version which has not been fully edited and content may change prior to final publication. Citation information: DOI 10.1109/OJAP.2024.3477318

MARZIEH MEHRI DEHNAVI was born in Isfahan, Iran, in 1986. She received the B.Sc. degree in Electrical Engineering from Isfahan University of Technology (IUT), in 2009 and the M.Sc and Ph.D. degrees in Electrical Engineering from Polytechnique Montreal, Canada, in 2015 and 2021, respectively. Currently, she is senior RF engineer with DELL in Canada. Her research interest includes microelectronics, RF and antenna design.

JEAN-JACQUES LAURIN was born in Repentigny, Canada, in 1959. He became Member of IEEE in 1986, Senior Member in 1998 and Life Member in 2024. He received the B. Eng. degree in Engineering Physics from Polytechnique Montreal in 1983, and the MASc and PhD degrees in Electrical Engineering from the University of Toronto in 1986 and 1991 respectively. He joined Polytechnique Montreal in 1991, first as a researcher, and then as a professor in the Department of Electrical and Computer Engineering in 1992. He is a founding member of the Poly-Grames Research Centre and was the Co-Director of STARaCom, a Quebec-based research cluster in radiofrequencies and communications, from 2017 to 2023. He retired and became Adjunct Professor in 2024. His research contributions include topics in electromagnetic compatibility, antenna design for aerospace applications and microwave tomography. He has been a visiting researcher at Ecole Polytechnique Fédérale de Lausanne, ESTEC (European Space Research and Technology Centre of ESA), MDA and Universidad Politecnica de Madrid.

This work is licensed under a Creative Commons Attribution-NonCommercial-NoDerivatives 4.0 License. For more information, see https://creativecommons.org/licenses/by-nc-nd/4